

Multi-Phase Dusty Gas in the Center of NGC 4278

Yuping Tang^{1*}, Qiusheng Gu[†], Shuinai Zhang, Baitian Tang

¹*Department of Astronomy, Nanjing University, Nanjing 210093, P. R. China*

Key Laboratory of Modern Astronomy and Astrophysics (Nanjing University), Ministry of Education, Nanjing 210093, China

6 November 2021

ABSTRACT

We present the Spitzer spectroscopic mapping observations toward the central kpc region of the nearby elliptical LINER galaxy, NGC 4278, by using the Infrared Spectrograph (IRS). These observations reveal rich mid-IR emission features of extended ionized gas, warm molecular hydrogen and dust. Different phases of gas and dust are closely related and belong to a same elongated feature. We further study properties of multi-phase dusty gas to uncover the underlying mechanism of ionization and excitation. The band ratio and intensity of PAH features in the central region might reflect modified size distribution resulted from selective destruction. H_2 S(0)-S(7) pure rotational lines of molecular hydrogen show excessive intensity and moderately high excitation temperature comparing with photon dissociation region (PDR). A strong and extended [SiII] emission line is detected, which could be a sign of reduced depletion of silicon in interstellar dust. We also discover an extended high ionization region associated with enhanced H_2 S(1) emission. We conclude that a shock-heating component is required to account for observed emission characteristics, which could be triggered by cloud-cloud interactions during accretion of cold gas from the large HI disk.

Key words: galaxies: active - galaxies: elliptical and lenticular,cD - galaxies: nuclei - infrared: galaxies - NGC 4278

1 INTRODUCTION

A uniform, old stellar population plus extremely hot gas ($T \sim 10^6 - 10^7$ K) were considered the only components of elliptical galaxies historically. However, recent studies confirm that cold and warm diffuse matter are not rare — although generally small in amount — in these systems. The SAURON integral-field Survey of Early-Type Galaxies (Sazi et al. 2006) reported a 66 percent detection of extended emission gas for ellipticals, with a wide variety of spacial distributions and kinematic behaviors. Neutral hydrogen observations show that plenty of extended neutral hydrogen gas is clearly present in elliptical galaxies (Morganti et al. 2006; Noordermeer 2006). Moreover, even cooler interstellar medium (ISM) including dust and molecular gas has been detected at a modest level (Knapp et al. 1989; Lauer et al. 2005; Wiklind et al. 1995; Sage et al. 2007).

The origin of both warm and cold matter in nearby elliptical galaxies still remains controversial, clarifying this question is important for us to understand the ongoing physical

processes that drive the evolution of this class of systems. In many cases, the warm and cold gas are linked with each other in nearby ellipticals (Morganti et al. 2006; Serra et al. 2008), suggesting the two components might be different phases of a same structure. For emission gas, line ratios typical of LINERs are usually found in nearby ellipticals (Ho et al. 1997; Filippenko, 2003). A variety of mechanisms have been applied to interpret its energy source. Besides photoionization by active nucleus and low level residual star formation, possibilities of photoionization by an old, hot stellar population (Binette 1994; Macchetto et al. 1996), cooling flow or thermal interaction with hot gas (Sparks et al. 1989; de Jong et al. 1990; Fabian, 1994) and heating via shocks (Doptia & Sutherland, 1995) were also discussed and examined by previous authors, while a conclusive answer has not yet been reached. On the other hand, the lack of any significant correlation between the cold diffuse matter and stars on both mass and kinematics in nearby ellipticals might be a sign of external origin for the former content (Knapp et al. 1985; Goudfrooij & de Jong, 1994; Oosterloo et al. 2002), although the continuous thermal and dynamical evolution of ellipticals, such as heating of stellar ejecta through random collision, might assist to obscure such a relationship.

* E-mail: tangyping@gmail.com

† E-mail: qsgu@nju.edu.cn

The nearby ($D = 16.1\text{Mpc}$; Tonry et al. 2001), isolated elliptical galaxy NGC 4278 is a rare sample of ellipticals with detections of multi-phases ISM, thus offering a significant opportunity to study the evolution of gaseous matter in such environment. As among the first ellipticals detected of cold gas, NGC 4278 has long been known for its massive ($\sim 10^8 M_\odot$), regular HI disk extending beyond 5kpc . Furthermore, the detection of CO emission is recently reported by Combes et al. (2007). Strong emissions produced by ionized gas are revealed by the SAURON survey (Sazi et al. 2006), which kinematically coincides well with the HI disk (Morganti et al. 2006) and show asymmetrical sub structures with high ionization. In optical images, NGC 4278 shows large scale dust patches located north and north-west of the galaxy center (Lauer et al. 2005), which might contribute to excess far-infrared emission detected by IRAS (Knapp et al. 1989) and ISO (Temi et al. 2004) infrared space telescopes. Besides, mid-infrared extended, non-stellar emission possibly related to reprocessing of UV/optical radiation by polycyclic aromatic hydrocarbons (PAHs) is shown in Spitzer IRAC image after removing the stellar contribution (Tang et al. 2009).

In this work, we present mid-infrared spectral mapping observations of Spitzer Space Telescope toward the central kpc region of NGC 4278. There are several reasons why spatially resolved mid-infrared spectroscopy in such area is interesting. First, it allows us to carry out analysis on spectra without suffering from serious dust extinction; second, the uniform spectral and spacial stellar background of elliptical galaxy provide us chances to identify activities characterized by low surface brightness; third, mid-infrared spectra contain emission features from multi-phase ISM, including dust, warm molecular hydrogen as well as ionized gas, thus enable us to explore the underlying heating mechanism from various aspects. Our ultimate goal is to understand the origin and evolution of cold and warm matter in this LINER galaxy.

This paper is organized as follows: The observation and data reduction are described in Section 2. The emission line maps are shown in Section 3. We explore the physical properties of cold and warm matter from observations in Section 4 and carry out discussion on possible energy source behind the diffuse matter in Section 5. In Section 6 we draw our conclusions.

2 OBSERVATION AND DATA REDUCTION

We download the IRS Basic Calibrated Data (BCD) of NGC 4278 from the archive of Spitzer Science Center (Program ID:30471, PI: J.D. Smith). This program is aimed to investigate the nature of PAH emission features in nearby galaxies hosting low-luminosity AGN. The observations were obtained in low resolution spectral mapping mode with a spectral resolution $R \sim 60-130$, using the Short-Low ($5-15\mu\text{m}$) and Long-Low ($14-38\mu\text{m}$) modules and taken on February 09, 2007.

The SL spectral mapping covers 1×10 map positions with a step size of $1.85''$ in perpendicular direction. Observations consist of 60s-ramp duration with 3 circles per step. The observations obtained by LL module consist of 4×11 map positions with a step size of $5.08''$ in the perpendicular

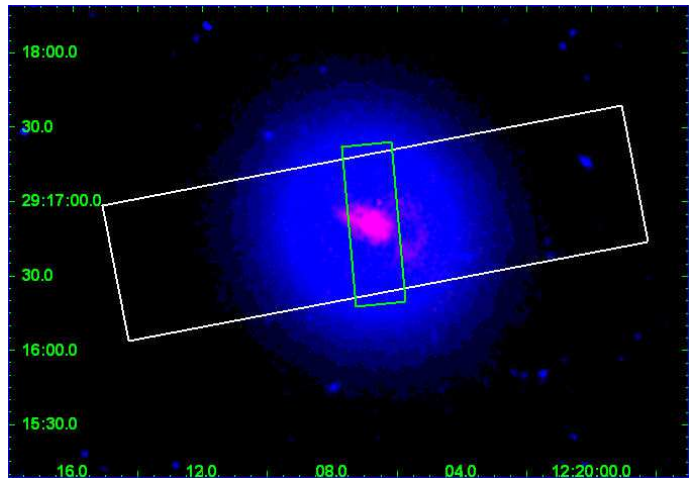


Figure 1. Mapping area of NGC 4278. Blue: IRAC3.6 image. Red: IRAC8.0 non-stellar emission, derived by subtracting a scaled IRAC3.6 image from IRAC8.0 image (Tang et al. 2009). White box: Mapping coverage of long slit observations. Green box: Mapping coverage of short slit observations.

direction and a step size of $15.0''$ in the parallel direction, 30s-ramp duration was used with 1 circle per step. The mapping area is shown in Figure 1.

Primary data reduction were done by Spitzer Science Center (SSC) pipeline, version S18.7.0 for both SL and LL modules, including standard reductions such as removing of electron bias, dark current subtraction and flat-field correction. We further use the IDL-based software package CUBISM (Smith et al. 2007a) to extract and combine spectra into a single spectral cube. Background subtraction was done by using off-source observations (rouge) accompanied with each map, which were taken in a region containing no spectral signatures by the same slit pattern and exposure time with the mapping sequence. After background subtraction, the major artifacts remaining in the two-dimensional map of the data cube are some bright “stripes”, which are caused by bad pixels rastered across the map. The bad pixels are removed by carefully examining each wavelength of the panel with the backtracking tool in the CUBISM.

3 EMISSION LINE DISTRIBUTION

Ionized gas in NGC 4278 has been previously studied by Sarzi et al. (2006, 2010) based on the observations of SAURON survey. Figure 2 shows the distribution of $[\text{OIII}]\lambda 5007$ emission obtained by SAURON observations (kindly provided by Marc Sarzi) overplotted with the contours of IRAC $8\mu\text{m}$ excess non-stellar emission, the latter is obtained by subtracting a scaled IRAC $3.6\mu\text{m}$ image from the IRAC $8\mu\text{m}$ image. In Tang et al. (2009), We’ve shown that for quiescent ellipticals, $[3.6] - [8.0]$ color are generally constant and change little with radius from the center. We can simply multiply 3.6 image by a constant to account for the contribution of an old stellar population at $8.0\mu\text{m}$, then degrade this image to $8.0\mu\text{m}$ and subtract it from the original $8\mu\text{m}$ image. For NCG 4278, this constant, which reveals the infrared-color of an old stars, is taken as 0.29. The

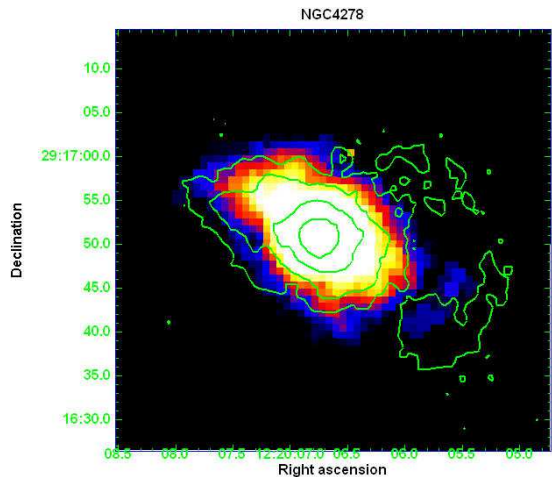


Figure 2. [OIII] λ 5007 emission line map, overlaid with contours of IRAC 8.0 non-stellar emission. Contour levels are given as: 1.50, 0.61, 0.25, 0.10 (in units of MJy/sr).

central elongated feature along south-west to north-east direction with a position angle of 70° generally coincides with [OIII] λ 5007 distributions. Both [OIII] λ 5007 and H_β emission are further spatially and kinematically consistent with the inner part of HI disk in NGC 4278 (Morganti et al. 2006), suggesting that dust, cold gas and warm gas simply belong to different phases of a same gaseous rotational structure.

Another important result of SAURON observations for NGC 4278 is a “reverse” distribution of ionization states for warm gas in the central region. The nuclei shows a lower degree of ionization comparing with the outer circumnuclear region. In Figure 3 we present the map of [OIII] λ 5007/ H_β ratio along with the IRAC $8\mu\text{m}$ non-stellar emission. A low-surface brightness, high ionization ring-like structure extends beyond $10''$ and is obvious seen in the south and west area. This feature, together with the fact that the radial profile of H_β flux is more extended than expected for photoionization by the central AGN (Sarzi et al. 2010), strongly suggest a second ionization source dominates over the area outside the central $5''$. The IRAC $8\mu\text{m}$ non-stellar emission also shows extended patchy structures to the west of the main feature. As already noticed by the Sarzi et al., the western patchy structures seem to be anti-correlated with the distribution of ionization degree, with some sub-areas of low PAH $7.7\mu\text{m}$ covering having the highest [OIII] λ 5007/ H_β ratio. The authors suggested this feature could be explained by the local hardening of ionizing continuum and the decline of ionization parameter due to dust effect. It is interesting to notice that, there is no such area with irregular [OIII] λ 5007/ H_{β} distribution on the north-east side of the main elongated structure, where the surface brightness of $8\mu\text{m}$ excess is higher than patchy regions.

We construct line maps from Spitzer mapping observations by applying standard spectral decomposition method (PAHFIT) on each pixel. Details on PAHFIT will be discussed in Section 4. We also compare each emission line map with IRAC $8\mu\text{m}$ non-stellar emission. To do this, we first degrade the resolution of IRAC 8.0 image to that of each line map by gaussian convolution. The scale of the gaussian

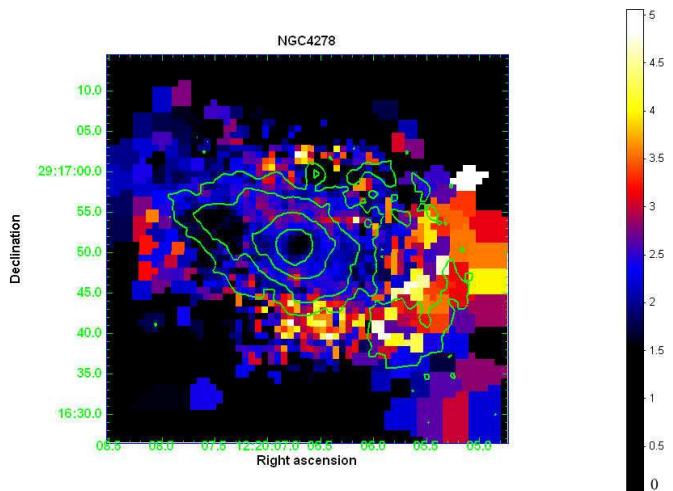


Figure 3. Line ratio map of [OIII] λ 5007/ H_β , overlaid with contours of IRAC 8.0 non-stellar emission. Contour levels are as in Fig 2.: 1.50, 0.61, 0.25, 0.10 (in units of MJy/sr)

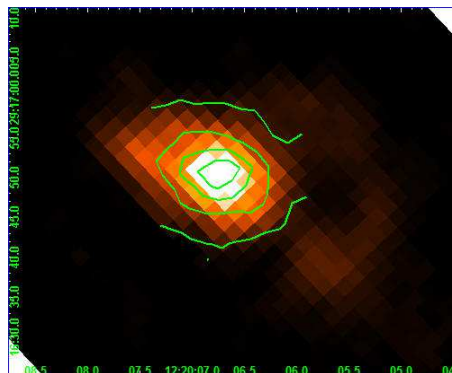


Figure 4. IRAC 8.0 non-stellar emission image, overlaid with contours of PAH11.3 contours. Contour levels are given as: 12.1, 8.54, 4.93, 1.33 (in units of 10^{-22}erg/s), where the lowest contour level corresponds to 3σ significance.

kernel is determined by matching PSF of IRAC 8.0 image with PSF at the wavelength of line center. After convolution, IRAC $8\mu\text{m}$ image is rebinned to the same pixel size of each line map.

In Figure 4 and Figure 5 we show distributions of PAH11.3 μm and PAH17 μm band emission respectively, overlaid on IRAC $8\mu\text{m}$ non-stellar emission. For PAH11.3 μm , the mapping area has not covered the entire PAH emission region. Nevertheless, the two distributions agree well with each other for the central elongated feature, supporting the validity of using latter distribution to trace PAH $7.7\mu\text{m}$ emission. The spacial distribution of PAH17, however, does not totally coincide with that of IRAC $8\mu\text{m}$ excess. PAH17 μm distributes in a more symmetrical pattern relative to IRAC $8\mu\text{m}$ excess.

In Figure 6 and Figure 7 we present the distribution of H_2 S(3) (mapped in SL module) and H_2 S(1) (mapped in LL module) pure rotational lines of molecular hydrogen. For S(3), the distortion of contours on the northern edge of the main feature results from removal of a series of severe global bad pixels and does not necessarily imply a true turbulence.

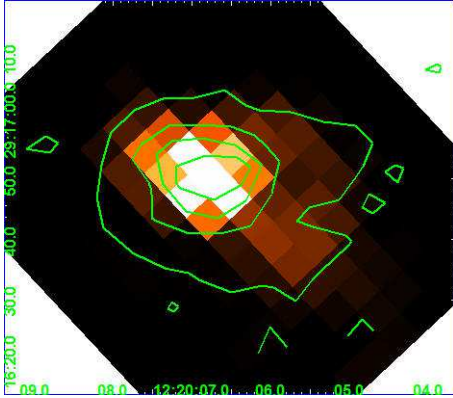


Figure 5. IRAC 8.0 non-stellar emission image, overlaid with contours of PAH17 contours. Contour levels are given as: 2.41, 1.67, 0.94, 0.20 (in units of 10^{-21} erg/s), where the lowest contour level corresponds to 3σ significance.

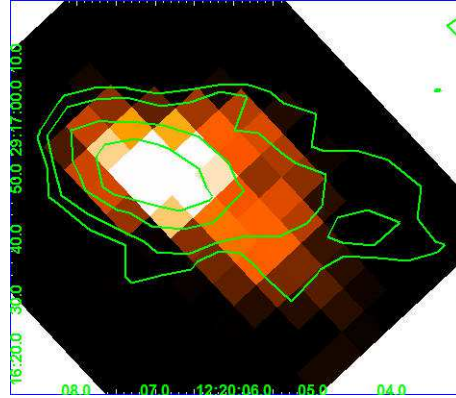


Figure 7. IRAC 8.0 non-stellar emission image, overlaid with contours of H_2 S(1) contours. Contour levels are given as: 4.10, 2.22, 1.09, 0.72 (in units of 10^{-22} erg/s), where the lowest contour level corresponds to 3σ significance.

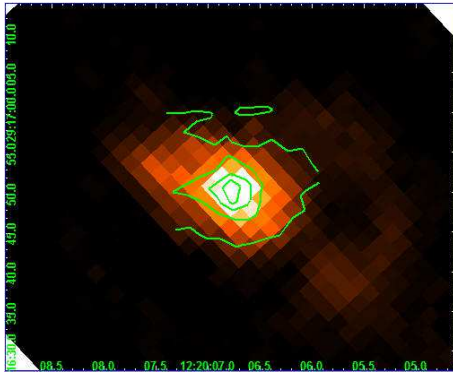


Figure 6. IRAC 8.0 non-stellar emission image, overlaid with contours of H_2 S(3) contours. Contour levels are given as: 4.73, 4.00, 3.31, 2.33, 1.81, 1.36, 0.38 (in units of 10^{-22} erg/s), where the lowest contour level corresponds to 3σ significance.

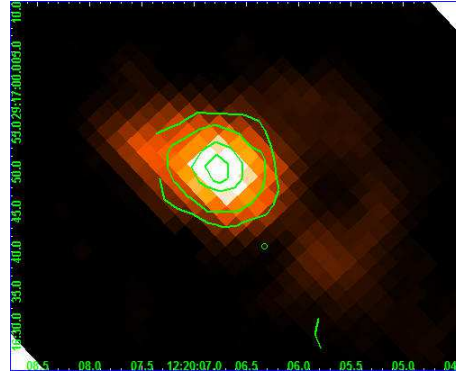


Figure 8. IRAC 8.0 non-stellar emission image, overlaid with contours of $[NeII]12.8\mu m$ contours. Contour levels are given as: 3.45, 1.70, 0.64, 0.29 (in units of 10^{-22} erg/s), where the lowest contour level corresponds to 3σ significance.

Still, it is obvious that both S(3) and S(1) emissions generally follow PAH emission. The H_2 S(1) distribution is slightly more extended than PAH patchy structures west of the main feature. We notice that the flux peak of H_2 S(1) map deviates from that of IRAC $8\mu m$ image by about $4''$, which is slightly smaller than the pixel size ($5.08''$) of LL orders and need to be further confirmed.

Figure 8-10 show distributions of fine-structure lines for $[NeII]12.8\mu m$, $[NeIII]15.6\mu m$ and $[SiIII]34.8\mu m$. With their ionization potential spreading over a wide range, ionized emission lines show considerable difference from PAH features and H_2 pure rotational lines. Especially, for high ionization line $[NeIII]$ (with an ionization potential of 41.0 eV), the central distributions are more symmetrical within the central $10''$ comparing with PAHs and warm molecular hydrogen emissions, although still showing a faint elongated feature consistent with the position angle of the latter two distributions. For the strong $[SiIII]$ emission (with a lower ionization potential of 8.2 eV), its sufficiently high S/N ratio reveals a more extended component, which departs from the extended patchy distribution of PAHs and H_2 S(1) emission.

In Figure 11, we present Chandra X-ray observations of the diffuse soft X-ray emission with point source being removed (which will be present in Zhang et al. in prepara-

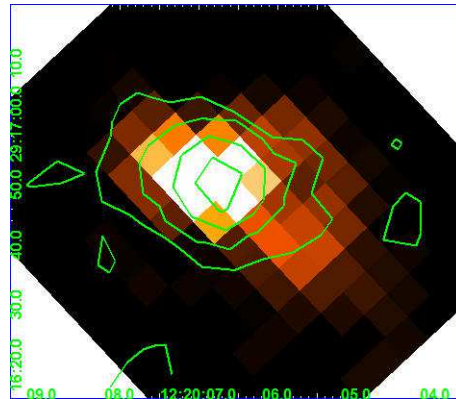


Figure 9. IRAC 8.0 non-stellar emission image, overlaid with contours of $[NeIII]15.6\mu m$ contours. Contour levels are given as: 6.34, 3.20, 1.31, 0.68 (in units of 10^{-22} erg/s), where the lowest contour level corresponds to 3σ significance.

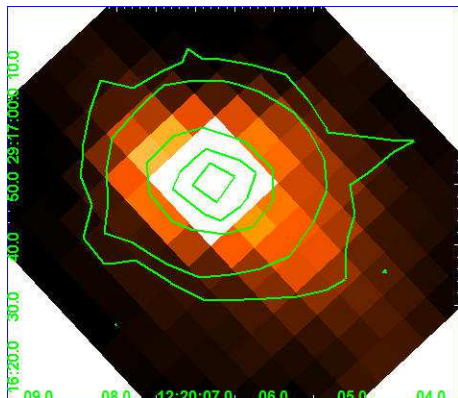


Figure 10. IRAC 8.0 non-stellar emission image, overlaid with contours of [SiII]34.8 μ m contours. Contour levels are given as: 16.60, 9.71, 4.80, 1.85, 0.87 (in units of 10^{-22} erg/s), where the lowest contour level corresponds to 3σ significance.

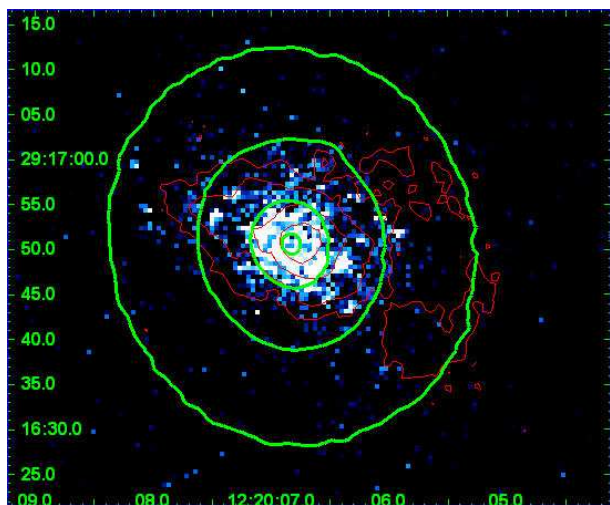


Figure 11. Chandra 0.2-1.5keV diffuse emission image removed from point sources, overlaid with contours of IRAC3.6 image (Green) as well as contours of IRAC8.0 non-stellar emission (Red). Contour levels of IRAC3.6 image are given as: 23.22, 6.46, 1.80, 0.50 (in units of MJy/sr). Contour levels of IRAC8.0 non-stellar emission are as in Fig 2.: 1.50, 0.61, 0.25, 0.10 (in units of MJy/sr).

tion), overlaid with the contours of IRAC 3.6 emission as well as the IRAC 8 non-stellar emission. While lacking an extended X-ray halo, the bulk of diffuse emission is confined to the central region and is generally consistent with the distribution of IRAC 8.0 non-stellar emission. The elongated feature of X-ray diffuse emission has previously been noticed by Terashima et al. (2003), this coincidence with warm gas might suggest a connection between the two phases of gaseous matter in the center. We also notice that recently, Younes et al. (2010) find a temperature of 0.4 ± 0.1 keV for thermal component in the central $10''$ region.

4 SPECTRA OF NUCLEAR AND EXTENDED REGIONS

Spectra of the nuclear region are extracted from a 8-arcsec circular aperture centered at the surface brightness peak of the continuum. The mid-infrared emission in NGC 4278 is extended, we need to use slit loss correction function (SLCF here after) to correct the original flux calibration provided by SSC based on point-source, which overestimates the flux by neglecting the flux accepted from outside the slit. Currently the SLCF is built on a simple assumption that the extended emission is uniform and unlimitedly extended (Smith et al. 2007a). Unfortunately, this assumption is not well satisfied in the case of NGC 4278, which shows a considerable degree of surface brightness concentration. The application of the SLCF leads to two artifacts in the spectra. First, a significant mismatch appears at the boundary of SL2 and LL1, where flux density of SL1 is 20% higher than LL2. This mismatch happens because the slit width and pixel size in LL module is nearly three times as in SL. At the same wavelength, the SLCF would overcorrect LL spectra in comparison with SL, because the real “excess” flux coming from outside the slit is relatively less in LL due to concentration of the extended emission. Another artifact would be more complex. Since the SLCF depends on PSF sizes at different wavelengths, application of this correction would modify the spectral profile. We estimate these two effects by following steps. First, we directly match LL to SL by multiplication, this spectrum will be referred as “Matched Spectrum” hereby. Second, we disable the SLCF for LL spectra, this would elevate LL spectra by about 17% at the blue end, thus fill the gap between SL and LL, then we do a minor adjustment to scale LL to SL by multiplication. The resulted spectrum is called “Uncorrected Spectrum” hereby. The two spectra are shown in Figure 12. The disagreement between the two spectra is lower than 10% blueward of 20μ m but becomes significant at longer wavelengths. In this work, three lines of interest, H_2 S(0), [SiII]33.5 μ m and [SiII]34.8 μ m, fall on wavelengths longer than 20μ m, discussions depending on relative strengths involved with these lines will be treated with caution.

We further compared the spectra with IRAC and MIPS photometry results derived from a same aperture. For the data reduction of IRAC data, we started from the BCD images and followed the same steps as we did in Tang et al. (2009), for MIPS data, we started from the post-BCD image. We employed the extended source aperture correction for calibration developed by Tom Jarrett¹. For MIPS image, unfortunately, such a correction is not available. Thus we only give an estimation of lower and upper limit from the data. The lower limit is derived by directly integrating the counts within the aperture without an aperture correction, while the upper limit is derived by employing an aperture correction for point source, as provided in MIPS INSTRUMENT HAND BOOK², since such an aperture correction ignores the diffraction light from outside the aperture, it would over-estimate the real flux. The results are shown in Figure 12. The IRAC photometry points are consistent with our spectra within calibration uncertainty ($\sim 10\%$, Fazio et

¹ <http://spider.ipac.caltech.edu/staff/jarrett/irac/calibration/>

² <http://ssc.spitzer.caltech.edu/mips/mipsinstrumenthandbook/>

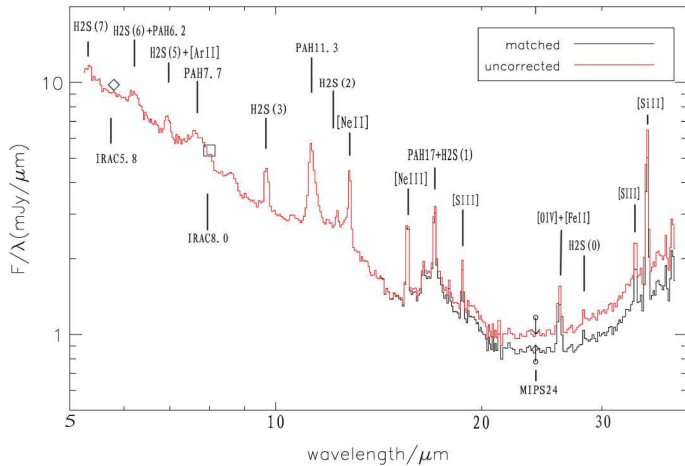


Figure 12. Spectra extracted from the central 8'' aperture, overplotted with IRAC5.8(diamond), IRAC8.0(square) and MIPS24(circle plus arrow) photometry data points. Black solid line is the Matched Spectrum with LL orders corrected by SLCF, red solid line is the Uncorrected Spectrum with LL orders uncorrected by SLCF.

al. 2004), indicating the flux calibration based on SLCF is reliable for SL observations. The MIPS photometry data fails to help distinguish between the Matched Spectrum and the Uncorrected Spectrum.

Hereafter, we will carry out discussions based on results from the Uncorrected Spectrum, since the mismatch between the SL and LL modules indicates that the SLCF correction based on the assumption of uniform extended source is not proper for LL observations. We caution the readers that this approach is not a precise solution. Nevertheless, this will not bring significant influence on the spectral shape shortward of $20\mu\text{m}$, although might overestimate lines flux by no larger than 30% at the longest wavelength (For [SiII] $34.8\mu\text{m}$, the line flux derived from the Uncorrected Spectrum is 29.3% higher than that from the Matched Spectrum.).

We use the package PAHFIT (Smith et al. 2007b) to fit the full $5 - 38\mu\text{m}$ spectrum. PAHFIT applies three sets of components (thermal continuum produced by stars and dust; PAH features; emission lines of ion species and molecular hydrogen) to separate different emission components. Throughout this article, the error bars are directly given by CUBISM and PAHFIT. In CUBISM, only BCD-level statistical uncertainty estimates produced by the IRS pipeline from deviations of the fitted ramp slope are considered when building error cubes, other uncertainties are not taken into consideration (Smith et al. 2008). The errors for combined quantities, such as integrated intensities, estimated are formulated using the full covariance matrix by CUBISM (Smith et al. 2007b), which is based on Levenberg-Marquardt algorithm. It should be noticed that systematic calibration uncertainty is not accounted for here. We estimate it to be not larger than 10% by comparing SL spectra with IRAC 5.8 μm and 8.0 μm monochromatic flux density (Figure 12). However, in this research, most discussions are based on relative strength of spectral features, where calibration uncertainty cancels out. The result of spectral decomposition is shown in Figure 13. Generally, the observation could be success-

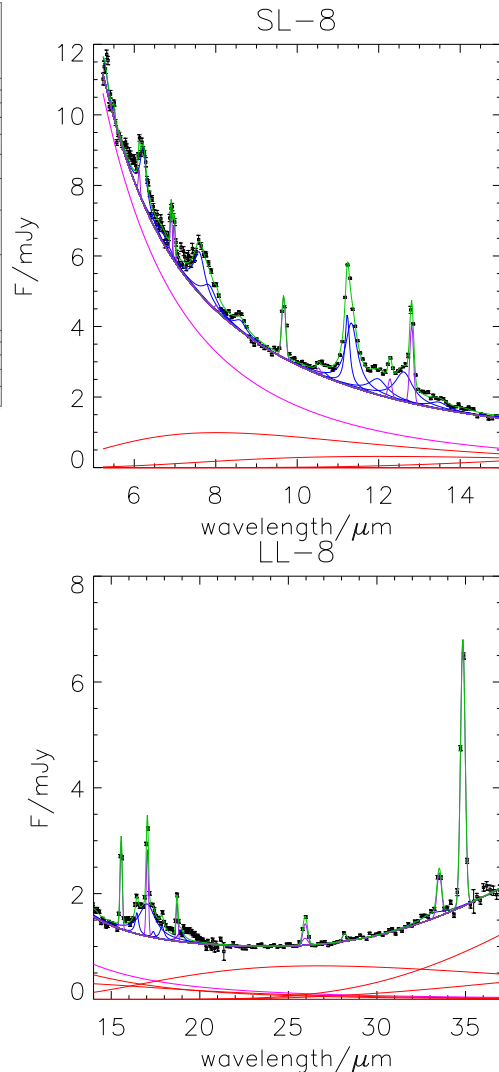


Figure 13. Full decomposition of Uncorrected Spectra extracted from the central 8'' aperture. The magenta line shows the stellar continuum, red solid lines represent the multi-temperature thermal dust components, the grey line is the summation of the stellar and dust continuum. Blue lines show PAH emission features, violet lines represent emissions arising from warm molecular hydrogen and ionized species. Up: $5 - 15\mu\text{m}$, Down: $15 - 37\mu\text{m}$.

fully reproduced by combination of various components. The spectrum shows no sign of silicate absorption around $10\mu\text{m}$, coinciding with the result derived from Balmer Decrement (Ho et al. 1997). The only significant spectral feature unable to be constructed by models is the $18 - 20\mu\text{m}$ plateau possibly caused by large PAH molecules, simply because PAHFIT excludes this feature from consideration. Smith et al. (2007b) suggested this plateau-like extension is not correlated with PAH $17\mu\text{m}$ feature. Another potential problem underlying the procedure of PAHFIT is that it only considers silicate absorption. As pointed out by Bregman et al. (2006) and Kaneda et al. (2008), for early type galaxies, silicate emission feature around $10\mu\text{m}$ originated from the circumstellar envelope of asymptotic giant branch (AGB) stars might affect the measurement of PAH feature at $7.7\mu\text{m}$. This effect will be estimated in the next section.

The nuclear spectra of NGC 4278 are somehow beyond

Table 1. Emission Line Strengths in the Central 8" Aperture

Line	$Flux(m)^a$ ($10^{-21} W/cm^2$)	$Flux(uc)^b$ ($10^{-21} W/cm^2$)
PAH6.2 μm	22.60 \pm 0.74	22.50 \pm 0.74
PAH7.7 μm	41.30 \pm 2.46	40.80 \pm 2.47
PAH11.3 μm	38.60 \pm 0.24	38.60 \pm 0.24
PAH12.6 μm	17.20 \pm 0.48	17.00 \pm 0.49
PAH17 μm	22.00 \pm 0.39	23.80 \pm 0.48
H ₂ S(0)	0.40 \pm 0.04	0.48 \pm 0.06
H ₂ S(1)	4.27 \pm 0.10	4.48 \pm 0.13
H ₂ S(2)	1.56 \pm 0.07	1.56 \pm 0.07
H ₂ S(3)	6.26 \pm 0.09	6.26 \pm 0.09
H ₂ S(5)	3.53 \pm 0.27	3.53 \pm 0.27
H ₂ S(6)	1.80 \pm 0.22	1.80 \pm 0.22
H ₂ S(7)	0.83 \pm 0.24	0.84 \pm 0.24
[Ar II]7.0 μm	2.78 \pm 0.26	2.78 \pm 0.26
[S IV]10.5 μm	0.62 \pm 0.09	0.62 \pm 0.09
[Ne II]12.8 μm	6.14 \pm 0.09	6.13 \pm 0.09
[Ne III]15.6 μm	4.82 \pm 0.11	4.95 \pm 0.14
[S III]18.7 μm	1.50 \pm 0.07	1.65 \pm 0.09
[S III]33.5 μm	1.88 \pm 0.07	2.39 \pm 0.10
[SiII]34.8 μm	11.00 \pm 0.09	14.10 \pm 0.15

^a Spectra with LL orders corrected by SLCF and matched to SL orders.^b Spectra with LL orders uncorrected by SLCF.

the ordinary elliptical galaxies for its abundance of emission features. In contrast, the continuum generally follows a blackbody radiation from an old stellar population, with some marginal contribution from hot and warm dust. The emission features appearing in the mid-infrared spectra of NGC 4278 could be divided into three groups, pure rotational emission lines of molecular hydrogen, forbidden emission lines of ions and PAH emission features. In the following sections, we extract physical information from each set of lines, then we will discuss possible energy origin of emission features implied by properties of the gaseous matter.

4.1 PAH Emission Features

Detection of PAH emissions is uncommon for elliptical galaxies, which could naturally be explained by rapid destruction due to sputtering by hot plasma. Nevertheless, as mentioned before, NGC 4278 is devoid of a X-ray halo. While strong PAH emissions are always related with star-forming activities (Wu et al. 2005), this might not necessarily be the case in elliptical galaxies, since significant amount of UV photons could be expected for an old stellar population (Binette et al. 1994; Greggio & Renzini et al. 1990). In some limited cases reported by now, such as Bregman et al. (2006a) and Kaneda et al. (2008), PAH emission features in ellipticals show obvious difference from galaxies with active star-formation. The band ratio of 7.7 μm emission feature arising from CC stretching vibrations of PAHs, to 11.3 μm feature arising from CH out-of-plane bending vibrations could be lower significantly than star-forming regions. This is also the case for NGC 4278, with $I_{7.7}/I_{11.3} = 1.07$. Kaneda et al. (2008) pointed out that while using PAHFIT to derive PAH emission flux, silicate emission feature around 10 μm originated from outflow winds of AGB stars could lead to

significant underestimation for PAH 7.7 feature. When this feature is subtracted from the original spectrum of NGC 4278, the continuum on the long wavelength side of PAH7.7 will be depressed, thus PAH 7.7 flux derived from fitting will increase significantly, especially when PAH 7.7 emission is weak. To estimate this effect, we subtract a template of quiescent elliptical galaxy after scaling it to our spectrum at 5.5 μm (which is an average of three quiescent ellipticals: NGC 1407, NGC 1549 and NGC 3904, kindly provided by Hidehiro Kaneda), the resulted PAH 7.7 emission doubled in flux and gave $I_{7.7}^*/I_{11.3} = 2.03$. In comparison, the median value of $I_{7.7}/I_{11.3}$ is about 4 for HII dominated sources in SINGs sample (Smith et al. 2007b), with a minimum around 2.

In actively star-forming galaxies, PAH band ratio of 7.7/11.3 has been suggested to reflect the relative proportion of ionized PAHs to neutral PAHs (Galliano et al. 2008), which is further controlled by intensity of UV radiation field, electron density and temperature. Meanwhile, temperature distribution of PAHs could also affect PAH band ratios, while higher average temperature generally lead to stronger emission at shorter wavelength. It is still in argument, however, which factor controls PAH band ratio in non star-forming regions, such as elliptical galaxies or AGNs. Smith et al. (2007b) compare HII sources with AGNs in SINGs sample, they found lower ratios of $I_{7.7}/I_{11.3}$ and $I_{11.3}/I_{17}$ for PAH emissions in AGNs and also lower ratio of the PAH luminosities to total infrared luminosities for AGNs. All these facts are consistent with the scenario that the selective destruction of small PAH molecules and the resulted shift of temperature distribution toward lower temperature are responsible for PAH band ratios in AGNs. This viewpoint is supported by O'Dowd et al. (2009), who used optical diagnostics to clarify AGNs and star-forming galaxies and found

that the PAH band ratios behave as the destruction of small PAH molecules becomes important in AGNs. In this sense, NGC 4278 is consistent with the AGN population in all respects. The band ratio $I_{11.3}/I_{17} = 1.75$, also falls in the AGN region of Smith et al. 2007. We further estimate the ratio of total PAH luminosity to total infrared luminosity. Following Dale et al. (2002) and Smith et al. (2007b), we obtain the total infrared luminosity based on MIPS observations at 24, 70, 160 μm (data taken from Temi et al. 2009). Then we calibrate the TIR luminosity to 8" aperture based on MIPS 24 luminosity derived from the spectrum. The result gives a $L_{totalPAHs}/L_{TIR} = 4.7\%$, which is lower than HII galaxies in SINGs sample (with a median $\sim 10\%$, and a minimum $\sim 8\%$ for HII galaxies with metallicity $12 + \log(O/H) > 8.1$).

4.2 Warm Molecular Hydrogen

Mid-IR molecular hydrogen quadrupole emission lines arising from pure rotational transitions are clearly detected in the central region of NGC 4278. These lines are effective coolants for warm molecular gas with temperature $\sim 100 - 1000K$. Excitation mechanisms of H_2 emissions include radiative decay after pumping to electronically excited states through absorption of ultraviolet photons (Morton & Dinerstein, 1976); inelastic collision with other particles (Martin et al. 1996; Everett & Pogge, 1997); reformation onto excited states for dissociated molecular gas (Hollenbach & Micke, 1989). Due to low critical densities ($< a few \times 10^3 cm^{-3}$ for S(0)-S(3)), transitions between lower levels are usually thermalized through collisional de-excitation, making pure rotational lines alone not guaranteed diagnostics to distinguish between different excitation mechanisms.

The radiative decay within pure rotational levels of molecular hydrogen follows quadrupole selection rules, only $\Delta J = -2$ could occur, where J is the rotational quantum number. The flux of a certain transition could be expressed as $F_{ul} = A_u N_u h \nu_{ul} \Omega / 4\pi$, where $u=l+2$, A_u is the Einstein A coefficient of the upper level, N_u is the column density of molecules on the upper level, $h\nu_{ul}$ is the photon energy and Ω is the beam solid angle. Under the assumption of local thermalization equilibrium (LTE), the fraction of molecules in each states to total column density could be written as $N_u/N_{total} = g_u \exp[-E_{ul}/kT]/Z(T)$. Where g_u is the statistical weight, given by $g_u = (2I+1)(2l+1)$, here $I=0$ for even u and $I=1$ for odd u . $Z(T)$ is the partition function. We adopt $Z(T) = 0.0247T/[1 - \exp[6000K/T]]$ (Herbst et al. 1996), which is valid for $T > 40K$.

Figure 14 shows the excitation diagram for the central 8" region of NGC 4278. Emission lines up to S(7) are detected above 3σ level, except S(4), which could be obscured by PAH7.7 feature. The fit of S(6) is highly affected by the adjacent 6.2 micron PAH feature. We estimate the uncertainty of S(6) by fitting 100 randomly noise-added spectra within noise limit, the result estimated in this way is in consistent with that directly derived from PAHFIT, with a mean flux of $1.8 \times 10^{-21} erg/s$. Data points in our diagram do not show obvious sign of ortho-to-para ratio (OPR) deviating from thermal equilibrium below $J = 8$ level, which would appear as a "zigzag" pattern between ortho states and para states (Neufeld et al. 2006). We thus use a two temperature model with $OPR = 3$ (equilibrium value) to fit all data points. The result gives a warm component $T_w \sim 197K$

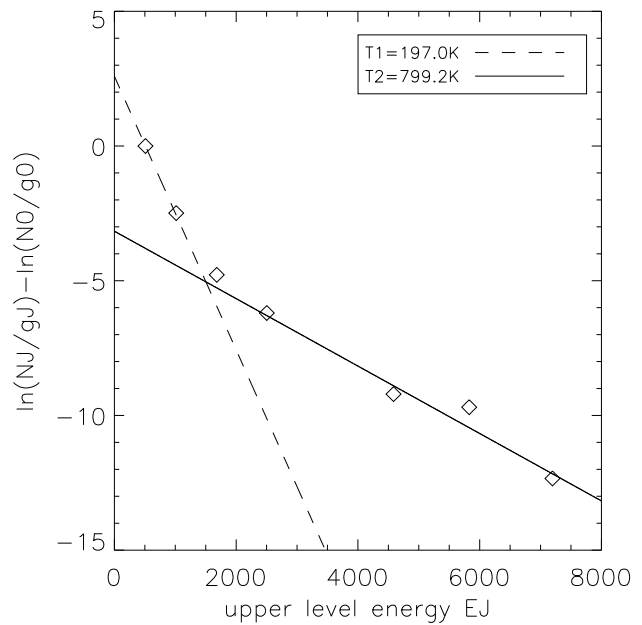


Figure 14. Excitation diagram of H_2 pure rotational lines. The dash line represents a temperature of 197.0K, the solid line represents a temperature of 799.2K. The data point of H_2 S(4) is not shown, since it is blended with PAH8.6 μm features and could not be accurately decomposed.

with with column density $N_{Hw} = 0.75 \times 10^{20} cm^{-3}$ and a hot component ($T_h \sim 799K$) with $N_{Hh}^{hot} = 1 \times 10^{18} cm^{-3}$, corresponding to a mass of $1.49 \times 10^6 M_\odot$ within 8" aperture. This result remains almost unchanged if we apply lines derived from the "Matched Spectrum", which lowers S(1) by 10% and S(0) by 18%, the two temperature given in this case is $T_w \sim 206K$ and $T_h \sim 811K$.

Roussel et al. (2007) carried out a systematic research on H_2 pure rotational emissions based on SINGs galaxies sample, they suggest that H_2 rotational lines in nearby star-forming galaxies are dominated by emission from photon dissociation regions (PDR), while in AGN objects excess H_2 emissions could be excited through shock heating. In NGC 4278, molecular hydrogen shows a higher excitation temperature than most galaxies in SINGs sample, in which only three galaxies classified as AGN objects are detected of lines higher than S(3). To compare NGC 4278 with SINGs galaxies, we follow Roussel et al. (2007) and use only S(0)-S(3) to fit a two temperature model, which gives a warm component $T_w \sim 189K$ with $N_{Hw} = 2.1 \times 10^{20} cm^{-3}$ and a hot component $T_h \sim 701K$ with $N_{Hh} = 4 \times 10^{18} cm^{-3}$. The temperature of the warm component and the fraction of the hot component are still higher comparing with most SINGs galaxies. Meanwhile, this temperature is lower than stellar scale shock-heated region, such as supernova remnants (Neufeld et al. 2007; Hewitt et al. 2009) and Herbig-Haro objects (Neufeld et al. 2006), but similar to some recently discovered galaxy-scale shocks (Appleton et al. 2006; Ogle et al. 2007). Furthermore, CO emissions have been detected in NGC 4278 with IRAM observations (Combes et al. 2007). This allows us to calculate the fraction of warm H_2 to cold H_2 . We assume that the excitation temperature

of warm H_2 keeps constant and calibrate the mass from 8" aperture to 23" aperture based on the flux of H_2 S(1), 23" is the beam size of IRAM to derive cold H_2 mass. The result gives $M(\text{warm } H_2)/M(\text{cold } H_2)=0.10$, somehow larger than the typical value in SINGs sample.

A three temperature model would not achieve a significantly better result, this is because energy levels higher than $J = 7$ do not lie along a straight line and could not be fitted by a simple temperature component. One possible explanation is that S(6) line ($J=8$) is overestimated, since this line is blended with [ArII] emission and might not be well decomposed. Otherwise, if S(6) and S(7) are measured accurately, higher rotational levels with $J > 7$ might indicate a OPR lower than 3. Unfortunately, without a reliable measurement of S(4), which is blended with PAH8.6 feature, we are not able to discern between different possibilities.

4.3 Fine-structure Line emission

The nuclear spectra of NGC 4278 show abundant emission lines arising from low-level forbidden transitions of different ionic species, including [ArII]7.0 μm , [SIV]10.5 μm , [NeII]12.8 μm , [NeIII]15.6 μm , [OIV]&[FeII]26 μm blend, [SIII]18.7 μm , [SIII]33.5 μm as well as [SiII]34.8 μm . These lines provide valuable information about physical states of warm gas. The ratio of [NeIII]/[NeII] is commonly used as an indicator of ionization states, which shows a value of 0.81 for the nuclear region of NGC 4278. This is a typical value found in LINER objects and cannot help distinguish among starforming regions, AGN and shock-heated regions (Allen et al. 2008, Dale et al. 2009).

The most distinctive feature of the fine-structure emissions in NGC 4278 is the strong [SiII]34.8 μm emission located at the red end of the spectrum, which could be compared with the nearby [SIII]33.5 μm line and shows a ratio of [SiII]34.8 μm /[SIII]33.5 μm =5.9. This ratio is higher than any of SINGs galaxies (Dale et al. 2009) and resemble values observed in shock-dominated regions, such as supernova remnants (Neufeld et al. 2007) and large scale shock triggered by galaxies interaction (Cluver et al. 2010), in which [SiII] emission is boosted by sputtering destruction of dust during fast-shock, since as an element of high depletion, a large fraction of Si is locked in dust in diffuse ISM. Dale et al. (2009) find a separation of [SiII]/[SIII] ratio between AGNs and HII galaxies in SINGs sample while AGNs show stronger [SiII] emissions. In their discussion, this separation might be caused by reduced depletion of silicon, X-ray photoionization process or an increased density for emission gas. The last possibility, however, seems unlikely to be applicable to NGC 4278. The electricity density derived by the ratio of [SIII]18.7 μm /[SIII]33.5 μm , with a value of 0.69, is close to the low density limit and indicates the bulk of the fine-structure emissions come from regions with density around 300 cm^{-3} (Giveon et al. 2002). On the other hand, it is also doubtful that X-ray photoionization plays a major role in boosting [SiII] emission in the nuclear region of NGC 4278, which holds a LLANG with a moderate hard X-ray luminosity $L_{2-10keV} = 10^{40.4} erg/s$, since as mentioned above, the ionization of extended gas is not dominated by AGN photoionization, and [SiII] line distribution shows a widely extended structure, we will see in Section 4.5 that

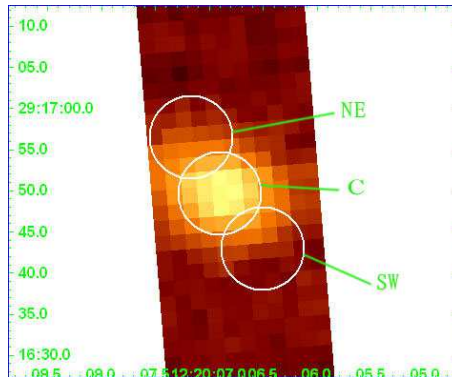


Figure 15. PAH11.3 map, overplotted with three neighbouring extraction apertures, each has a 5" radius: North-East(NE, centered at 185.02986,29.28235), Central(C, centered at 185.02875,29.28048), South-West(SW, centered at 185.02872, 29.27872).

high [SiII]/[SIII] ratio still appears in area more than 1kpc away from the nuclei.

4.4 Radial Emission-Line Distributions

It is important to understand the excitation mechanism of the extended emission in the central region. However, results given above are based on the spectra extracted from the central 8" aperture and could not avoid being mixed with an AGN component. It is thus very useful to further quantitatively explore the spatial distributions of different emission features. Unfortunately, both the limited mapping area of the SL module as well as the imperfect calibration for extended emission pose obstacles to this purpose. In this section, we extract spectra from three adjacent apertures of 5" radius, with one centered at the continuum peak of the spectral map and two centered at the northeast and southwest of the galaxy center, as shown in Figure 15. The 5" aperture size is somehow small for extraction of LL orders due to its large pixel size and extended PSF, comparing radial distribution of different lines based on LL observations should be taken with caution. Therefore, here we only focus on SL spectra. The spectra are presented in Figure 16 and the detected line fluxes are shown in Table 2.

While [NeIII]15.6 μm /[NeII]12.8 μm is a comfortable indicator of ionization states, [NeIII] falls on the LL wavelength range. Here we use [SIV]10.5 μm /[NeII]12.8 μm as a substitute for diagnostic of gas ionization. The validity of this approach has been verified by Groves et al. (2008). We find that the [SIV]/[NeII] in the two extended regions, say, NE and SW regions, are higher than the central region, although in both cases the [SIV] fluxes are barely higher than the 3 σ level. The [SIV]/[NeII] ratio is 0.16 in NE region and 0.24 in the SW region, in comparison with 0.08 in the central region. This result is consistent with the distribution of [OIII] λ 5007/ H_β derived from SAURON observations and confirm that a significant fraction of extended emission is not excited by central AGN photoionization even within the central 10" region.

It is also interesting to explore any possible variation of PAH band ratio in three regions. However, we found that PAH6.2/PAH7.7 ratios directly derived from PAHFIT in

Table 2. Emission Line Strengths in 3 Neighboring 5" Apertures

Line	NE ($10^{-21} W/cm^2$)	C ($10^{-21} W/cm^2$)	SW ($10^{-21} W/cm^2$)
PAH6.2 μm	3.63 ± 0.12	8.63 ± 0.14	2.79 ± 0.15
PAH7.7 μm	16.05 ± 1.06	51.77 ± 1.10	12.86 ± 1.03
PAH11.3 μm	8.67 ± 0.17	22.10 ± 0.15	5.96 ± 0.13
PAH12.6 μm	2.83 ± 0.29	9.03 ± 0.30	3.04 ± 0.12
H ₂ S(2)	0.33 ± 0.04	0.98 ± 0.05	0.15 ± 0.04
H ₂ S(3)	1.21 ± 0.05	4.08 ± 0.06	0.79 ± 0.06
H ₂ S(5)	0.74 ± 0.15	2.46 ± 0.18	< 0.34
H ₂ S(6)	0.44 ± 0.14	1.15 ± 0.14	0.49 ± 0.14
H ₂ S(7)	< 0.43	0.75 ± 0.15	< 0.46
[ArII]7.0 μm	< 0.54	2.34 ± 0.17	< 0.36
[SIV]10.5 μm	0.16 ± 0.05	0.33 ± 0.06	0.16 ± 0.05
[NeII]12.8 μm	1.00 ± 0.04	4.46 ± 0.06	0.67 ± 0.03
9.0 μm^a	7.85 ± 0.21	20.40 ± 0.23	6.01 ± 0.18

^a 9.0 Continuum Flux Densities are given in units of mJy.

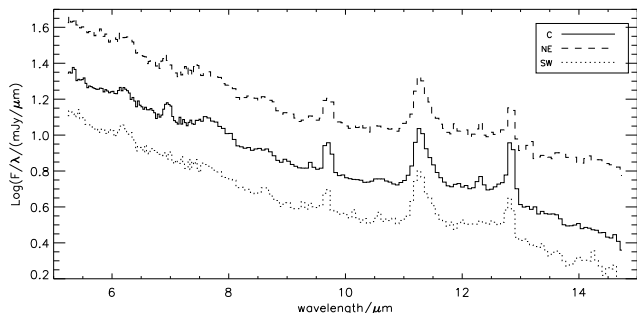


Figure 16. Scaled SL spectra extracted from the three apertures shown in Fig 14. The solid represents the result from the central aperture, the dash line represents the result from the north-east aperture, the dot line represents the result from the south-west aperture.

three regions are larger than 0.5 and cannot be explained by any PAH model (Draine & Li, 2001). We suggest such an unphysical value of PAH6.2/7.7 appeared because we failed to consider the silicate emission as we did in Section 4.1, thus underestimated PAH7.7 flux. With a template of silicate emission being subtracted from original spectra, the fitting results are given in Table 2. Our results show that both PAH6.2/7.7 and PAH7.7/11.3 do not have significant spatial variation, while PAH 6.2/7.7 is slightly lower in the center and PAH7.7/11.3 is higher in the center. This may suggest more large, neutral PAHs in the galaxy center relative to the outer area, which could be a result of either hard radiation process by AGN or shock process while gas flow into the center.

In Figure 17, we show pixel-to-pixel comparisons between [NeII]12.8 μm , PAH11.3 μm and H₂ S(3) for central 11 \times 9 pixels of SL map. It is obvious that [NeII]12.8 μm shows distinct slope changes for most luminous 9 pixels, which correspond to a central region of about $< 3''$. This should be a sign that AGN continuum starts to dominate the heating in this region and produces relative more high ionization nebula line emissions relative to PAHs emissions and

warm molecular emissions. This result confirms SAURON result that [OIII] $\lambda 5007/H_\beta$ starts to decline as entering central 5" area. Another sign revealed by Figure 17 is enhanced H₂ S(3) emission toward the outmost area, relative to both [NeII] and PAH11.3, which appears as a shallower slope in H₂ S(3) to PAH11.3 μm plot and excessive H₂ S(3) in [NeII]12.8 μm to H₂ S(3) plot. Enhanced H₂ S(3) toward the outter area is consistent with our finding that H₂ S(1) is more extended than both PAH emissions and nebula lines.

4.5 Spectra in Western High-Ionization Region

We further explore the ionization and excitation states for gas in the western high-ionization, low surface brightness region as revealed by SAURON observation. We extract LL spectra from a 8" aperture centered at the west of the nuclei, as shown in Figure 16. Unlike the nuclear region, here we employ SLCF to correct spectra since there should be considerable outcoming light from the nearby bright nuclear region diffracted into local area. The spectrum is given in Figure 17, comparing with spectrum extracted from the central area. For high-ionization region, the continuum emission longer than 20 μm show a shallower slope than spectra of the central region, this difference remains when we compare it with the SLCF-corrected central spectrum, which, as discussed above, flattens the continuum longer than 20 μm . We can quantify the slope longer than 20 μm continuum simply by the ratio of final fitted continuum at 36 μm to that at 21 μm . For central region with slit loss correction, F36/F21=2.7, for central region without SLCF, F36/F21=3.1, while in high ionization region, the ratio is 1.9. The lack of a hot dust component, as indicated by shallower continuum could be a natural result of weaker UV-optical continuum or larger sizes of local dust grain.

The high-ionization region is characterized by an enhanced H₂ S(1) emission. The relative strength of H₂ S(1) to nearby [NeIII]15.6 μm , [SIII]18.7 μm ionized emission and underlying PAH17 μm feature in high-ionization region is increased by a factor of 2 or more. Meanwhile, the excitation temperature derived from H₂ S(1) and H₂ S(0) is $> 183K$.

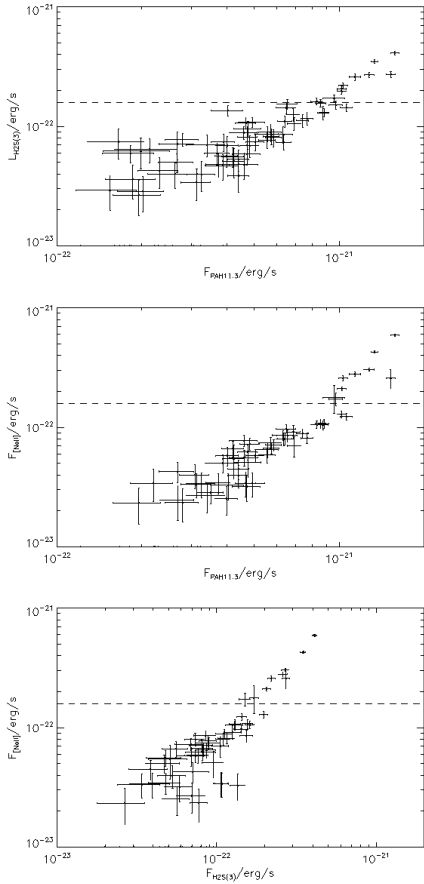


Figure 17. Pixel-to-Pixel plots for central 9×11 pixels of SL mode spectral map. Upper panel: $\text{H}_2 \text{ S}(3)$ to PAH11.3. Middle panel: [NeII] to PAH11.3. Lower panel: [NeII] to $\text{H}_2 \text{ S}(3)$. Dash line mark pixels where slope starts to change.

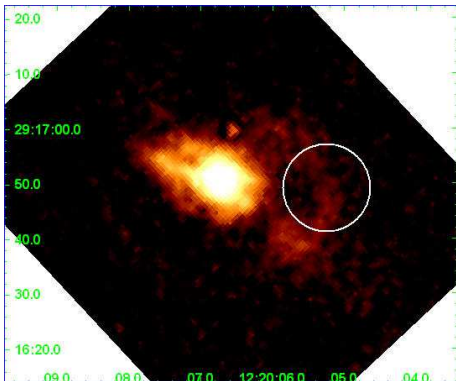


Figure 18. Image of IRAC8.0 non-stellar emission, overplotted with the extraction aperture for high ionization region, which is centered at (185.02190, 29.28036), with a radius of $8''$.

Without information from higher level lines, this result indicates a temperature not lower than the central region if assuming an equilibrium OPR. The enhancement of $\text{H}_2 \text{ S}(1)$ is consistent with what has been shown in Figure 6, the distribution of $\text{H}_2 \text{ S}(1)$ narrow band emission exhibits an extended component to the west of the nuclei, in the next section, we will discuss possible origin of this feature.

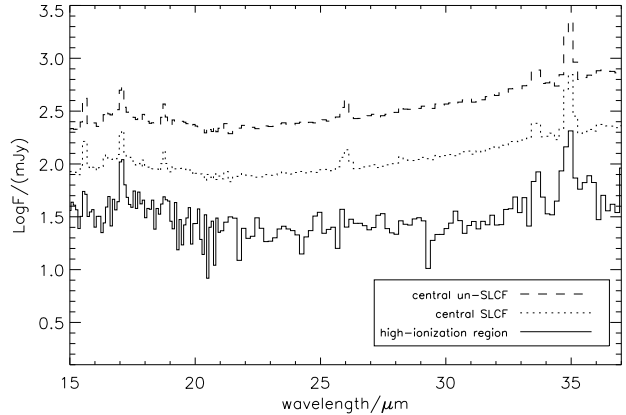


Figure 19. Scaled LL spectra (solid) extracted from the aperture shown in Fig 17. For comparison, Central $8''$ Matched Spectra (dot line) and Uncorrected Spectral (dash line) are scaled and plotted.

Table 3. Emission Line Strengths in the High-Ionization Region

Line	Flux (10^{-21} W/cm^2)
PAH17 μm	2.24 ± 0.38
$\text{H}_2 \text{ S}(0)$	< 0.12
$\text{H}_2 \text{ S}(1)$	0.85 ± 0.07
[NeII]15.6 μm	0.30 ± 0.06
[SIII]18.7 μm	< 0.19
[SIII]33.5 μm	0.26 ± 0.06
[SiII]34.8 μm	0.95 ± 0.10

5 DISCUSSION: THE ORIGIN OF EXTENDED WARM GAS AND DUST

Results from Spitzer mapping observations reveal abundant warm dust, molecular gas and ionized gas in the central region of NGC 4278. One or more additional ionization sources apart from AGN photoionization are required to explain the extended ionized gas. It is conceivable that energy source responsible for extended warm gas should also be related to the physical properties of extended dust and molecular hydrogen we observed. In this section, we will discuss possible heating mechanisms that could offer a self-consistent explanation for the different phase of extended dusty gas.

Both the detections of PAHs and cold molecular gas might imply some degree of residual starformation, while it seems unlikely that starforming activity plays an important role in the case of NGC 4278. Infrared emission lines NGC 4278 show distinct behavior from that should be expected for PDR region (Kaufman et al. 2006). Besides, barely any sign of starforming activity is shown at any wavelength in the central kpc region. Galax observations show that NGC 4278 should be classified as a typical UV upturn galaxy based on its strong FUV emission throughout the galaxy, this is a direct evidence that the background radiation field is possibly from a hotter old stellar population (post AGBs,

LMXBs or EHBs) instead of OB stars. Second, in Sarzi M., Shields, J. C., Schawinski K. et al. (2010), the authors have quantitatively explored the ionization mechanism for NGC 4278 based on comparison between emission line diagnostic and predictions of MAPPING-III models (Section 3.4.1, Figure 12). Their results show that ionized gas in NGC 4278 clearly fall outside the starformation region in emission line diagram. The extended ionized gas in NGC 4278 exhibits LINER type emission lines, which further cast doubt on the idea that ionized gas is not heated by young stars.

As to stellar population analysis, previous research show different results for the stellar population of NGC 4278, while Serra P. et al. 2008 reported a 3Gyr single stellar population in a circumnuclear region of NGC 4278, Zhang Y. et al. 2008 and recent SAURON results (Kuntschner, H. et al. 2010) just gave a 10Gyr stellar population.

If the bulk of extended atomic, molecular and dust emission comes from starforming area, similar spacial distribution should be expected for different types of emission lines, such coincidence is also not observed, suggesting at least a second physical process should be acting.

Another commonly employed heating mechanism in elliptical galaxies is process related to X-ray emitting hot gas, such as cooling flow from hot gas and evaporation flow caused by interaction between cold and hot gas (Sparks et al. 1989; de Jong et al. 1990). Still, this possibility is easy to be ruled out. NGC 4278 shows no X-ray halo, and as could be seen in Figure 10, the diffuse soft X-ray emission in the central region seems to trace cold and warm gas and is too weak to serve as an efficient energy reservoir in order to explain the observed strong optical and infrared emission.

Based on SAURON results, Sarzi et al. (2010) suggest that warm gas in early-type galaxies are generally powered by evolved stellar sources, especially post AGB stars, based on their calculation that an old stellar population is able to provide sufficient ionizing photons for the observed warm gas, as well as the fact that surface brightness of H_{β} emission is tightly correlated with that of local optical continuum emission. The latter phenomenon was previously pointed out by (Macchetto et al. 1996). In Sarzi et al. (2010), the results have revealed the unusual ionization structure of NGC 4278. However, the dominant ionization source in NGC 4278 could still be photoionization by UV radiation from old stars instead of fast shock, based on the fact that high ionization regions are characterized by low surface brightness of H_{β} emissions, which contradicts with common case for shock-heated region. They also argued that the shock velocity predicted by shock models ($300 - 500 km/s$, depending on whether to introduce a HII precursor) is too large to maintain a stable rotational pattern as seen in NGC 4278.

Nevertheless, dynamical environment giving birth to hundred-to-thousand pc scale shock is not unexpected for the center of NGC 4278. As shown by Sarzi et al. (2006), the kinematic of ionized gas is different from that of stars, with its position angle of rotation axis showing a maximum deviation from that of the stars at the outmost region, while this misalignment angle between stars and gas gradually decreases toward the inner region and reach a minimum at the galaxy center. This kinematic feature is not difficult to understand. Morganti et al. (2006) point out that the central rotational structure of warm gas in NGC 4278 seems to be just a sub component of the large extended HI disk. It is

commonly recognized that massive cold gas disk in elliptical galaxies is usually a product of merging with a gas-rich galaxy. The faint tail-like features in HI map of NGC 4278 also support this idea. Therefore, shock triggered by random collisions between gas clouds could possibly happen when gas is accreted from the extended HI disk to the central stellar gravitational well. It is worthwhile to notice that, the western high ionization region shown in Figure 3 exactly corresponds to area in velocity map where gas experience turning of position angle (Sarzi et al. 2006).

Our observational results reveal several possible signs for a shock process happening in the central region of NGC 4278. As discussed above, the extended strong emission of [SiII] could explained by sputtering destruction of silicate dust grain in the fast shock process instead of X-ray photoionization by central AGN, this is further supported by possibly modified size distribution of PAHs, as implied by different PAH band ratios. Recently, Kaneda et al. (2010) show that in NGC 4589, another PAH-detected ellipticals sharing similar infrared spectral features with NGC 4278, the PAH17 distribution is different from that of PAH11.3 emission. The authors explain this segregation as that PAH11.3 arises from newly formed PAHs when dusty gas falling toward the center. In Figure 5 we find similar results, which may imply that PAHs are undergoing reprocessing in extended area. On the other hand, the X-ray diffuse emission spatially follows the main feature of ionized gas, molecular and dust. The temperature of thermal component found by Younes et al. (2010), $0.4 \pm 0.1 keV$ within $10''$ aperture, indicates a shock velocity of $\sim 600 km/s$ (Draine & McKee, 1993) and is higher than expected from optical line diagnostics. However, the authors also point out that the central diffuse emission may contain more than one temperature components, with a less-hot components in the extended region.

We find an excess luminosity of molecular hydrogen rotational lines populated in high excitation temperature comparing with that found in PDR regions of starforming galaxies, with respect to aromatic bands, $24\mu m$ continuum, Total IR luminosity as well as [SiII] $34.8\mu m$ emission (Roussel et al 2007). This component of extended warm molecular associated with highly ionized gas also provide a sign for extended shock. Enhanced emissions from warm molecular is found for AGN objects in SINGs sample and stellar/galactic scale shock-heated regions. Roussel et al. argue that X-ray excitation seems unlikely to be responsible for excess warm molecular hydrogen in SINGs AGN sub-sample, instead they suggest fast-shock triggered by dynamical perturbation as the heating source. Furthermore, we have found an extended high-ionization region related with enhanced H_2 S(1) emission. These facts support the idea that X-ray excitation from central AGN could not explain the observed excess, high excitation temperature H_2 emission. A second heating mechanism could be also supported by the possible deviation of H_2 S(1) peak from other lines as shown in Figure 6. On the other hand, there is no evidence of dynamical perturbation directly related with the central AGN. While being classified as a FR I radio galaxy, the radio jet of NGC 4278 is confined to milli-arcsec scale and shows a direction approximately perpendicular to the elongated main feature of warm gas (Falcke et al. 2000). The HST STIS high spacial resolution observations also indicate that the twist of veloc-

ity field only happens within the inner 0.5" region (Walsh et al. 2008).

Guillard et al. (2009) develop a common scenario to interpret the dominance of warm H₂ emissions in dynamically disturbed regions, in which pre-shock gas exists in both high density clouds and low-density intercloud gas. Under a higher shock velocity, the low-density, diffuse gas is heated to plasma with temperature a few $\times 10^6 K$, while the dusty clouds heated to lower than $10^6 K$ cool efficiently, dissipate their kinematic turbulent energy into H₂ emission through slow-shock. This scenario is consistent with our finding that the distribution of H₂ emission and PAH emissions are similar, while both of which depart from ionized emissions. It provides a natural explanation for the anti-correlation between $8\mu m$ PAH feature and [OIII] $\lambda 5007/H\beta$ shown in Figure 3, since PAHs is expected to be entirely destructed in fast-shock heated plasma (Micelotta et al. 2010). If so, the decreased [SiII]/[SIII] ratio in this region might be a result of relatively more pre-shock gas distributed in high density clouds.

It is uncertain, however, whether the shock component revealed by above evidences could be responsible for the bulk of gas ionization in the central elongated feature. The optical and infrared fine structure line diagnostics allowed by current data are not sufficient to clearly distinguish between UV photoionization and fast-shock. Although there are abundant optical spectral observations for NGC 4278 (Rose et al. 1984; Ho et al. 1997; Walsh et al. 2008), these observations are usually based on slit centered at the central AGN. We notice that due to detectable high excitation line [OIII] $\lambda 4363$ in its optical slit spectrum, NGC 4278 were suggested as an possible example of shock-excited LINERs (Rose et al. 1984). An obstacle to view shock-heating as a main ionization mechanism is the low surface brightness of high ionization area. Interestingly, we find a discrepancy between fine-structure lines with different ionization potentials, with the highest ionization mapped line, [NeIII] $15.6\mu m$, showing the most symmetrical distribution. A much lower [NeIII]/[NeII] is expected to be produced in shock region than in gas ionized by FUV radiation (Spinoglio & Malkan, 1992; Allen et al. 2008), if this feature is further confirmed, it implies that shock-heating may play a role in excitation of lower ionized species in extended region.

6 CONCLUSION

We performed the Spitzer IRS spectral mapping observations toward the central region of the nearby elliptical galaxy, NGC 4278. We discovered rich emission features produced by warm dust, molecular hydrogen and ionized gas in the galaxy center. The multi-phases of warm and hot gas generally coincide well with optical line distribution, suggesting they belong to a same structure. We confirm the reverse distribution of ionization states shown in optical observations. The spectrum of nuclear region is characterized by strong [SiII] $34.8\mu m$ emission, which is naturally explained by reduced silicon depletion through dust sputtering. The PAH band ratios in the nuclear region could be interpreted by modified size destruction under selective destruction, especially, the PAH $7.7\mu m/11.3\mu m$ ratio, decreases while moving away from the nuclei, indicating a high fraction of neu-

tral PAHs or a deficiency of small PAHs in the outer region. The warm molecular hydrogen shows excessive emissions arising from pure rotational transitions with respect to both dust and ionized emission lines, excitation diagram of pure rotational lines gives high excitation temperature similar to some galactic shock-heated regions. We found a high ionization extended region associated with enhanced rotational molecular emission. We conclude that a hundred-to-thousand pc scale shock region triggered by interaction between clouds and diffuse cold gas accreted from the outer region of the galaxy should exist under the dynamically perturbed environment in the center of NGC 4278, while the contribution of this shock component to the total ionization of gas is still unclear.

7 ACKNOWLEDGEMENTS

The authors are very grateful to Marc Sarzi and Hidehiro Kaneda for providing us SAURON data of NGC 4278 and IRS spectra of quiescent elliptical galaxies. This research made use of Tiny Tim/Spitzer, developed by John Krist for the Spitzer Science Center. The Center is managed by the California Institute of Technology under a contract with NASA. We would also like to acknowledge the financial support from the Natural Science Foundation of China under grants 10878010 and 10633040, and the National Basic Research Program (973 program No. 2007CB815405). This research has made use of NASA's Astrophysics Data System Bibliographic Services and the NASA/IPAC Extragalactic Database (NED), which is operated by the Jet Propulsion Laboratory, California Institute of Technology, under contract with the National Aeronautics and Space Administration. This work is based on observations made with the Spitzer Space Telescope, which is operated by the Jet Propulsion Laboratory, California Institute of Technology, under NASA contract 1407.

REFERENCES

- Allen M. G., Groves B. A., Dopita M. A., Sutherland R. S., Kewley L. J., 2008, *ApJS*, 178, 20
- Binette L., Magris C. G., Stasiska G., Bruzual A. G., 1994, *A&A*, 292, 13
- Bregman J. N., Temi P., Bregman J. D., 2006, *ApJ*, 647, 265
- Cluver, M. E., Appleton, P. N., Boulanger, F., et al. 2010, *ApJ*, 710, 248
- Combes F., Young L. M., Bureau M., 2007, *MNRAS*, 377, 1795
- Dale D. A. & Helou G., 2002, *ApJ*, 576, 159
- Dale D. A., et al., 2009, *ApJ*, 693, 1821
- de Jong T., Norgaard-Nielsen H. U., Jorgensen H. E., Hansen L., *A&A*, 232, 317
- Dopita M. A., Sutherland R. S., 1995, *ApJ*, 455, 468
- Draine B. T. & McKee C. F., 1993, *ARA&A*, 31, 373
- Everett M. E. & Pogge R. W., 1997, *IAUS*, 182, 106
- Fabian A. C., 1994, *ARA&A*, 32, 277
- Falcke H., Nagar N. M., Wilson A. S., Ulvestad J. S., 2000, *ApJ*, 542, 197
- Fazio G. G. et al., 2004, *ApJS*, 154, 10
- Filippenko A., 2003, in *ASP Conf. Ser.* 290, *Active Galactic Nuclei: From Central Engine to Host Galaxy*, ed. S. Collin, F. Combes, & I. Shlosman (San Francisco: ASP), 369
- Galliano F., Madden S., Tielens A. et al., 2008, *ApJ*, 672, 214

- Giveon U., Sternberg A., Lutz D., Feuchtgruber H., Pauldrach A. W. A., 2002, *ApJ*, 566, 880
- Goudfrooij P., de Jong T., Hansen L., Norgaard-Nielsen H. U., 1994, *MNRAS*, 271, 833
- Greggio L. & Renzini A., 1990, *ApJ*, 364, 35
- Groves B., Nefs B., Brandl B., 2008, *MNRAS*, 391, 113
- Guillard P., Boulanger F., Pineau D. F. G., Appleton P. N., 2010, *A&A*, 502, 515
- Ho L. C., Filippenko A. V., Sargent W. L. W., 1997, *ApJS*, 112, 315
- Herbst, T. M., Graham., J. R., Tsutsui, K., Beckwith, S., Matthews, K., Soifer, B. T. 1990, *AJ*, 99, 1773
- Hewitt J. W., Rho J., Andersen M., Reach W. T., 2009, *ApJ*, 694, 1266
- Hollenbach D. & McKee C. F., 1989, *ApJ*, 342, 306
- Jeong H. et al., 2009, *MNRAS*, 398, 2028
- Kaneda H., Onaka T., Sakon I., Kitayama T., Matsumoto H., Suzuki S., 2008, *ApJ*, 684, 270
- Knapp G., Guhathakurta R., Kim D.-W., Jura M. A., 1989, *ApJS*, 70, 329
- Knapp G. R., Turner E. L., Cunniffe P. E., 1985, *AJ*, 90, 454
- Lauer T. R., Faber S. M., Gebhardt K., et al., 2005, *AJ*, 129, 2138
- Macchetto F., Pastoriza M., Caon N., Sparks W. B., Giavalisco M., Bender R., Capaccioli M., 1996, *A&AS*, 120, 463
- Martin P. G., Schwarz D. H., Mandy M. E., 1996, *ApJ*, 461, 265
- Micelotta E. R., Jones A. P., Tielens A. G. G. M., 2010, *A&A*, 510, 36
- Morganti R., de Zeeuw P. T., Oosterloo T. A., McDermid R. M., Krajnovic D., Cappellari M., Kenn F., Weijmans A., Sarzi M. 2006, *MNRAS*, 371, 157
- Morton D. C. & Dinerstein H. L., 1976, *ApJ*, 204, 1
- Neufeld D. A., et al., 2006, *ApJ*, 649, 816
- Neufeld D. A., Hollenbach D. J., Kaufman M. J., Snell R. L., Melnick G. J., Bergin E. A., Sonnentrucker P., 2007, *ApJ*, 664, 890
- Noordermeer Edo, 2006, PhD thesis, Rijksuniversiteit Groningen
- O'Dowd M. J., 2009, *ApJ*, 705, 885
- Ogle P., Antonucci R., Appleton P. N., Whysong D., *ApJ*, 668, 699
- Oosterloo T. A., Morganti R., Sadler E. M., Vergani D., Caldwell N., 2002, *AJ*, 123, 7290
- Rose J. A. & Tripicco M. J., 1984, *ApJ*, 285, 55
- Sage L. J., Welch G. A., Young L. M., 2007, *ApJ*, 657, 232
- Sarzi M., 2006, *MNRAS*, 366, 1151
- Sarzi, M. et al., 2010, *MNRAS*, 402, 2187
- Serra P., Trager S. C., Oosterloo T. A., Morganti, R., 2008, *A&A*, 483, 57
- Smith J. D. T., Armus L., Dale D. A., Roussel H., Sheth K., Buckalew B. A., Jarrett T. H., Helou G., Kennicutt R. C. Jr., 2007a, *PASP*, 119, 1133
- Smith J. D., et al., 2007b, *ApJ*, 656, 770
- Sparks W. B., Macchetto F., Golombek D., 1989, *ApJ*, 345, 153
- Spinoglio L. & Malkan M. A., 1992, *ApJ*, 399, 504
- Roussel H., et al., 2007, *ApJ*, 669, 959
- Tang Y. -P., Gu, Q.-S., Huang, J.-S., Wang, Y.-P., *MNRAS*, 397, 1966
- Temì P., Brighenti F., Mathews W. G., Bregman J. D., 2004, *ApJS*, 151, 237
- Temì P., Brighenti F., Mathews W. G., 2009, *ApJ*, 695, 1
- Terashima Y., Wilson A. S., 2003, *ApJ*, 583, 145
- Tonry J. L., Dressler A., Blakeslee J. P., Ajhar E. A., Fletcher A. B., Luppino G. A., Metzger M. R., Moore C. B., 2001, *ApJ*, 546, 681
- Walsh J. L., Barth A. J., Ho L. C., Filippenko A. V., Rix H. -W., Shields J. C., Sarzi Marc., Sargent W. L. W., 2008, *AJ*, 136, 167
- Wiklund T., Combes F., Henkel C., 1995, *A&A*, 297, 643
- Wu H., Cao C., Hao C. -N., Liu F. -S., Wang J. -L., Xia X. -Y., Deng Z. -G., Young C. Ke-Shih, 2005, *ApJ*, 632, 79
- Younes G., Porquet D., Sabra B., Grosso N., Reeves J. N., Allen M. G., 2010, arXiv1004.5134

This figure "f9.jpg" is available in "jpg" format from:

<http://arxiv.org/ps/1101.0965v1>